

Cover Page



Universiteit Leiden



The handle <http://hdl.handle.net/1887/58472> holds various files of this Leiden University dissertation.

Author: Witte, W.E.A. de

Title: Mechanistic modelling of drug target binding kinetics as determinant of the time course of drug action in vivo

Issue Date: 2017-12-19

Chapter 6. Target and tissue selectivity prediction by integrated mechanistic pharmacokinetic-target binding and quantitative structure activity modelling

Anna H.C. Vlot^{*a}, Wilhelmus E. A. de Witte^{* a}, Meindert Danhof^a, Piet H. van der Graaf^{a,b}, Gerard J.P. van Westen^c, Elizabeth C. M. de Lange^{@a}.

^a Division of Pharmacology, Leiden Academic Centre for Drug Research, Leiden University, Einsteinweg 55, 2333 CC, Leiden, The Netherlands.

^b Certara Quantitative Systems Pharmacology, Canterbury Innovation Centre, Canterbury CT2 7FG, United Kingdom

^c Division of Medicinal Chemistry, Leiden Academic Centre for Drug Research, Leiden University, Einsteinweg 55, 2333 CC, Leiden, The Netherlands.

*These authors contributed equally

@ Correspondence: ecmdelange@lacdr.leidenuniv.nl

Manuscript under revision for the British Journal of Pharmacology

Abstract

Selectivity is an important attribute of effective and safe drugs, and prediction of *in vivo* target and tissue selectivity would likely improve drug development success rates. However, a lack of understanding of the underlying (pharmacological) mechanisms and availability of directly applicable predictive methods complicates the prediction of selectivity. We explore the value of combining physiologically based pharmacokinetic (PBPK) modelling with quantitative structure-activity relationship (QSAR) modelling to predict the influence of the target dissociation constant (K_D) and the target dissociation rate constant on target and tissue selectivity. The K_D values of CB1 ligands in the ChEMBL database are predicted by QSAR random forest (RF) modelling for the CB1 receptor and known off-targets (TRPV1, mGlu5, 5-HT1a). Of these CB1 ligands, Rimonabant, an inverse agonist at the CB1 receptor, CP-55940, a selective agonist for the CB1 and CB2 receptor and Δ^9 -tetrahydrocannabinol, one of the active ingredients of cannabis, were selected for simulations of target occupancy for CB1, TRPV1, mGlu5 and 5-HT1a in three brain regions, to illustrate the principles of the combined PBPK-QSAR modelling. Our combined PBPK and target binding modelling demonstrated that the optimal values of the K_D and k_{off} for target and tissue selectivity were dependent on target concentration and tissue distribution kinetics. Interestingly, in many cases the optimal K_D value is not the lowest K_D value, suggesting that optimisation towards high drug-target affinity can decrease the benefit-risk ratio. The presented integrative structure-pharmacokinetic-pharmacodynamic modelling provides an improved understanding of tissue and target selectivity.

Introduction

Selectivity is an important attribute of successful drugs since highly selective compounds are less likely to mediate side-effects.[1] On the other hand, targeting multiple targets simultaneously is increasingly considered as a valuable option to exert sufficient effect on a complex biological system.[2,3] Regardless of the desired degree of selectivity, understanding and prediction of the target binding to multiple targets in multiple tissues is essential for the optimisation of pharmacotherapy. In this article, we differentiate between two types of selectivity: target selectivity and tissue selectivity. Target selectivity is defined as a difference in target binding to different receptors and tissue selectivity is defined as a difference in target binding to the same target in different tissues. Additionally, a distinction is made between equilibrium selectivity and kinetic selectivity. Equilibrium selectivity refers to differential target binding while target binding is in equilibrium with the free drug concentration around the target. This equilibrium binding is described for single step target binding without target turnover according to Equation 1, in which K_D is the dissociation constant, $[L]$ is the unbound drug concentration, $[R]$ is the unbound target concentration, $[LR]$ is the bound drug-target complex concentration, k_{off} is the first order target dissociation rate constant and k_{on} is the second order target association rate constant.

$$(1) \quad K_D = \frac{[L] \cdot [R]}{[LR]} = \frac{k_{off}}{k_{on}}$$

Equilibrium target selectivity is thus driven by differential K_D values for the different targets. Kinetic selectivity, however, refers to a difference of the duration of target occupancy, which can be achieved by differential k_{off} values.[4] Differential k_{off} values do not always result in a differential duration of target occupancy *in vivo* since the plasma and local pharmacokinetics can also be rate-limiting for the duration of target occupancy.[5,6] As kinetic selectivity has previously been equated with differential k_{off} values[7], we will refer to differential k_{off} values as *in vitro* kinetic selectivity, while we will refer to an *in vivo* difference in the duration of target occupancy due to slow dissociation as *in vivo* kinetic selectivity.

A previous study that analysed a minimal mechanistic model for drug elimination, tissue distribution and target binding showed that an increase in drug-target affinity decreases the chance of observing *in vivo* kinetic selectivity, especially for slow tissue distribution and a high target concentration.[6] On that basis, it is expected that the optimal K_D for target and tissue selectivity is dependent on the target concentration, tissue distribution kinetics and binding kinetics. This contrasts with the current practice of drug discovery and development which often aims at a minimal value for the K_D and k_{off} and a maximal ratio to the off-target K_D and k_{off} value if selectivity is concerned.

The minimal mechanistic model that was analysed in the study of de Witte et al.[6] did not consider i) the effects of slow distribution of a drug into tissues where no target binding takes place nor ii) the limiting role that blood flow can have on tissue distribution. In order to capture the influence of these pharmacokinetic mechanisms, physiologically based pharmacokinetic (PBPK) models can be used. In these models, a distinction is made between system-specific properties and drug-specific properties. In this type of analysis, the values of system-specific parameters such as blood flows and volumes for each organ are based on the physiological literature data, while the values of drug-specific parameters, such as partition coefficients and protein binding are often based on *in vitro* data or on Quantitative Structure Activity Relationships (QSARs). [8] As such, these models allow the prediction of plasma and tissue unbound drug concentrations. The influence of drug-target binding on free drug concentrations has been described frequently with target-mediated drug disposition (TMDD) models. [9] The combination of PBPK and TMDD modelling has been reported in the literature previously but is not generally used in selectivity optimisation. [10–13] To obtain the drug-specific properties that determine the values of the partitioning parameters in PBPK models either experimental data for each individual drug or quantitative structure-activity relationships (QSAR) are required. These QSARs enable the prediction of partitioning parameters from the molecular structure. While these QSARs are often used in PBPK modelling to predict non-specific tissue distribution parameters, the prediction of specific target binding parameters is currently not incorporated in PBPK modelling, based on

the assumption that the amount of drug bound to its biological target is negligible relative to the total amount of drug in the body. [14–17]

QSAR models may be either regression or classification models which predict a response variable from a set of predictor values. In regression models, these predictor values are related to a continuous response variable (e.g. a K_D value), while in classification models the predictor values relate to a categorical variable (e.g. labelled “active” or “inactive”). The predictor values represent the molecular structure and molecular properties, and the response variable is an activity value, such as the K_D in the case of affinity. Machine learning methods such as support vector machines (SVMs), decision trees such as random forests (RFs) and deep neural networks (DNNs) are generally used to obtain a predictive learning model.[18–20] The training of these models is based on prior data, which means that their performance is greatly dependent on data quality and availability. A suitable database for bioactivity data is available in the ChEMBL, which can be used to obtain predictive QSAR models. [21,22]

Integration of drug-target binding prediction and pharmacokinetic modelling allows for the prediction of the selectivity profile for a given ligand directly from its molecular structure. As such, this modelling approach may provide information on a ligand’s efficacy and safety *in vivo* during the very early stage of drug development. This is especially relevant in systems that contain off-targets or targets that are also expressed in organs where no drug effect is desired. An example of the latter system is the cannabinoid system, of which the cannabinoid receptor CB1 is a major component. The CB1 receptor is widely expressed throughout the body but mainly found in the brain where it mediates a broad range of effects in health and disease. [23,24] Many off-targets have been identified for CB1 ligands, including the vanilloid receptor TRPV1, the metabotropic glutamate receptor mGlu5, and the serotonin receptor 5-HT1a. [25,26] Activity at these receptors, predominantly in the brain, may amplify or counteract effects at the CB1 receptor. TRPV1, for example, has been suggested to have an effect opposite of that of CB1 in anxiety and depression, which are common side effects observed for CB1 antagonists, and mGlu5 is a major player in the GABA-system, which is the target system for CB1 mediated therapies in Parkinson’s disease. [27–29] The mechanisms underlying functional *in vivo* selectivity are diverse and complex, but computational elucidation of off-target affinities and their integration in combined PBPK-TMDD modelling could help to identify safety concerns early in drug discovery and development, which would improve decision making in (pre)clinical drug development.

This article describes an approach towards the development of an integrative predictive modelling for drug selectivity. Firstly, the main determinants of *in vivo* equilibrium and kinetic selectivity, are identified by minimal PBPK-TMDD modelling and simulation. Secondly, the development and validation of a Random Forest based QSAR (QSAR-RF) model for the prediction of K_D values is described. Lastly, an example of the use of predicted K_D values in PBPK-TMDD modelling is provided for the combined *in vivo* target and tissue selectivity of Rimonabant, a prototype antagonist at the CB1 receptor.

Materials and Methods

1 Software

All simulations were performed in RStudio Version 1.0.136 coupled to R version 3.4.0. [30,31] Physicochemical property prediction and QSAR modelling were performed in Pipeline Pilot version 2016. [32]

2 Pharmacological Models

Three PBPK-TMDD models were developed: a minimal PBPK-TMDD model for simulation of target selectivity (**Model I, Figure 1**), a minimal PBPK-TMDD model for simulation of tissue selectivity (**Model II, Figure 2**), and an integrated brain PBPK-TMDD model for simulation of selectivity across brain regions and between targets using K_D values predicted in a QSAR-RF (**3.3 QSAR**) (**Model III, Figure 3**).

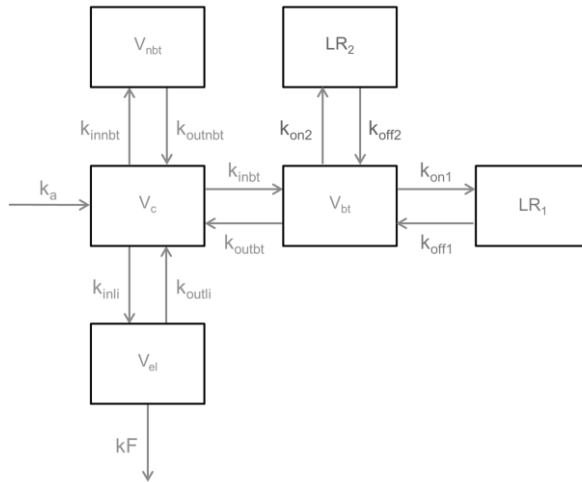


Figure 1. Schematic overview of the minimal target selectivity model (Model I). k_a = rate of absorption (h^{-1}), k_{in} = inwards distribution rate (h^{-1}), k_{out} = outwards distribution rate, k_{on} = association rate ($nM^{-1}h^{-1}$), k_{off} = dissociation rate (h^{-1}), kF = forward rate of elimination constant (h^{-1}), LR = ligand-receptor complex, V = tissue volume (L), nbt = non-binding tissue, c = central compartment, bt = binding tissue, el = eliminating tissue.

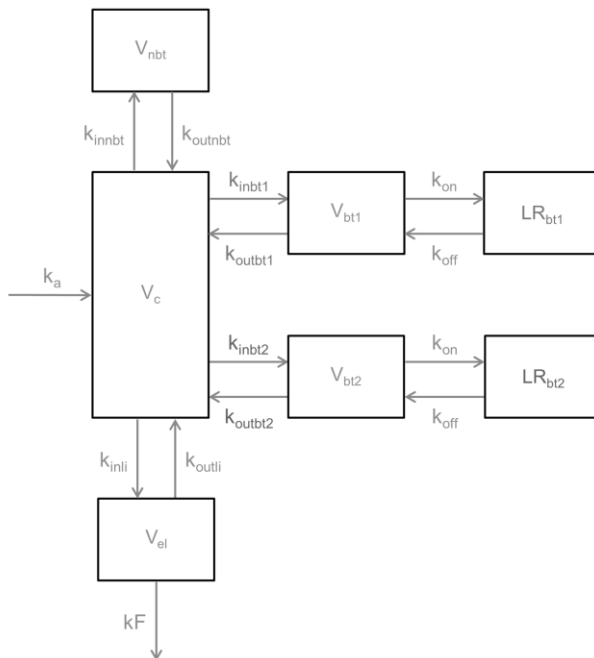


Figure 2. Schematic overview of the minimal tissue selectivity model (Model II). k_a = rate of absorption (h^{-1}), k_{in} = inwards distribution rate (h^{-1}), k_{out} = outwards distribution rate, k_{on} = association rate ($nM^{-1}h^{-1}$), k_{off} = dissociation rate (h^{-1}), kF = forward rate of elimination constant (h^{-1}), LR = ligand-receptor complex, V = tissue volume (L), nbt = non-binding tissue, c = central compartment, bt = binding tissue, el = eliminating tissue.

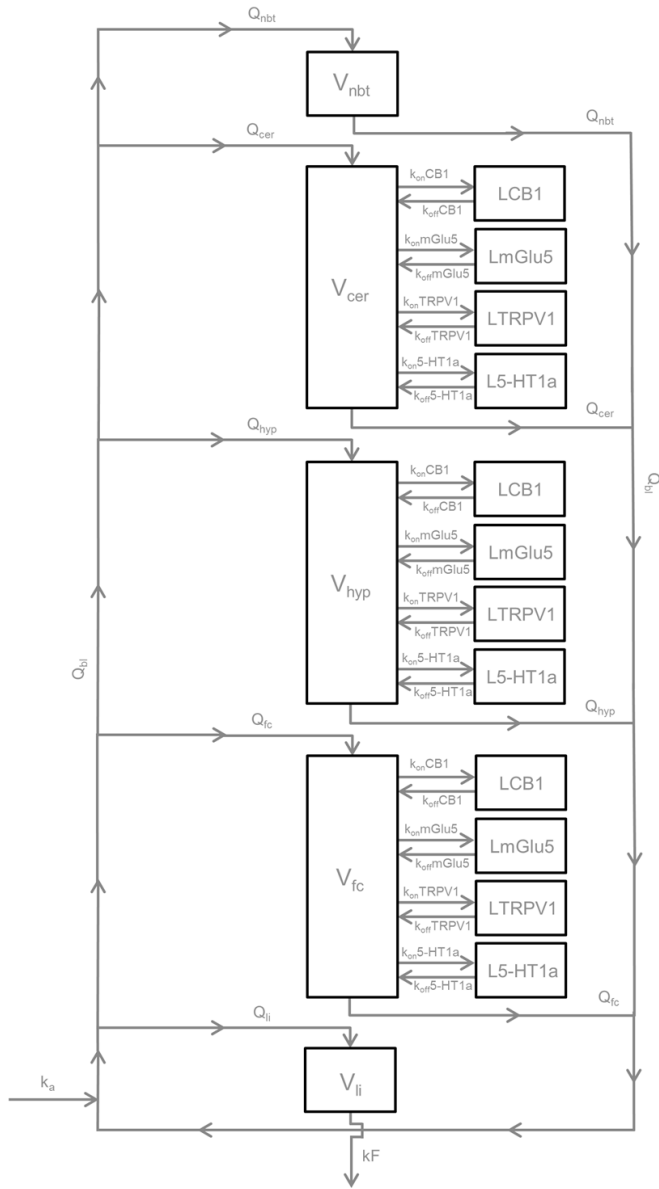


Figure 3. Schematic model of the brain PBPK-TMDD model. k_a = rate of absorption (h^{-1}), Q = blood flow (L/h), k_{on} = association rate ($nM^{-1}h^{-1}$), k_{off} = dissociation rate (h^{-1}), kF = forward rate of elimination constant (h^{-1}), LR (with $R = CB1$, $mGlu5$, $TRPV1$ or $5-HT1a$) = ligand-receptor complex, V = tissue volume (L), nbt = non-binding tissue, c = central compartment, bt = binding tissue, li = liver, cer = cerebellum, hyp = hypothalamus, fc = frontal cortex.

2.1 Parameters

2.1.1 Model I and II

All physiological values of the system-specific parameters were obtained from literature.[33–38] The heart was used as a reference organ for the determination of distribution into and out of the binding tissue. An overview of all model parameters is supplied in Supplemental 1.

2.1.2 Model III

All physiological values of the system-specific parameters were obtained from literature.[33–38] Target site distribution in the brain was characterized by the average effective flow through the target site as obtained from literature values from brain extra-cellular fluid flow to the cerebrospinal fluid as estimated for 9 drugs.[39] The conversion of these values as well as an overview of all parameters are supplied in Supplemental 1.

Receptor densities of CB1, mGlu5, TRPV1, and 5-HT1a in the cerebellum, hypothalamus, and frontal cortex were obtained from the literature for all four receptors, except the receptor concentration of mGlu5 in hypothalamus and 5-HT1a in cerebellum, which were not reported in the literature. [40–44] The mGlu5 receptor concentration in the hypothalamus was filled in with the averages of the other brain regions since differences between brain regions for the other receptors did not differ drastically. The 5-HT1a receptor concentration in cerebellum was set to the low value of 0.01 nM as it was reported to be unidentifiable.[43] Receptor concentrations in rats and humans were used interchangeably since no complete set of receptor densities could be obtained for either rats or humans. Values found in literature have shown to differ no more than ten-fold. [41,45] TRPV1 concentrations were given in ng/mg lysate and converted to pmol/mg protein by linear conversion. For this, the receptor concentration in ng/mg lysate and fmol/mg protein in the hypothalamus as reported in the literature was used. [42,46] The receptor density in the hypothalamus in fmol/mg was divided by the receptor density in ng/mg lysate and the resulting coefficient was used to transform the receptor density in ng/mg lysate of the cerebellum, hypothalamus and frontal cortex to the corresponding receptor density in fmol/mg. CB1 and TRPV1 concentrations in pmol/mg, were then converted to nM using a conservative (i.e. the lowest published) estimate of protein concentration in wet tissue of 100 mg/mL from literature. [47–49] An overview of the target concentrations is presented in

Table 1. An overview of the conversions and all target concentrations can be found in Supplemental 2.
Table 1. Receptor concentrations for the brain PBPK-TMDD model

	R_{tot,cer} (nM)	R_{tot,hyp} (nM)	R_{tot,fc} (nM)
CB1	527	248	529
mGlu5	5.1	16	25
TRPV1	19	13	12
5-HT1a	0.01	2.37	1.7

* cer = cerebellum, hyp = hypothalamus, fc = frontal cortex

Tissue-blood partition coefficients were calculated according to Poulin & Theil 2000 (**Equation (2)**). [50] The required physicochemical parameters (logP, logSo) [51] were determined in Pipeline Pilot. An overview of all parameters is supplied in Supplemental 3.

$$(2) P_{t:b} = \frac{[S_o * N_t] + [(S_w * 0.7 P_t) + (S_o * 0.3 P_t)] + [S_w * W_t]}{[S_o * N_b] + [(S_w * 0.7 P_b) + (S_o * 0.3 P_b)] + [S_w * W_b]}$$

where:

P_{tb} = predicted value of the tissue-blood partition coefficient

S_o = the solubility of the ligand in n-octanol (mol*m₃)

S_w = the solubility of the ligand in water (mol*m₃)

N_b = the neutral lipid content of blood (as fraction of blood volume)

N_t = the neutral lipid content of the tissue (as fraction of tissue volume)

P_b = the phospholipid content of blood (as fraction of blood volume)

P_t = the phospholipid content of the tissue (as fraction of tissue volume)

W_b = the water content of blood (as fraction of blood volume)

W_t = the water content of the tissue (as fraction of tissue volume)

2.2 Simulations

Model I

Model I was used to investigate the influence of K_D, target concentration (R_{tot}) and k_{off} on *in vivo* target selectivity. To this end, four different simulations (a,b,c,d) were performed. In all four simulations, the k_{off} at the first target (R1) was set to 0.01 h⁻¹ and the k_{off} at the second target (R2) was set to 10 h⁻¹ while both the K_D and R_{tot} were the same for both targets. An overview of the parameter values that were varied in these simulations can be found in **Table 2**. An overview of all other parameters can be found in Supplemental 1.

Table 2. Parameter values for *in vivo* target selectivity simulations with Model I.

	Model I				Model II			
	K_D	R_{tot}	k_{off} R1	k_{off} R2	K_D	R_{tot1}	R_{tot2}	k_{off}
a	10	25	0.01	10	10	25	0.025	10
b	0.01	25	0.01	10	1	25	0.025	10
c	10	0.25	0.01	10	0.1	25	0.025	10
d	0.01	0.25	0.01	10	0.01	25	0.025	10

* R1 is target 1, R2 is target 2, K_D and R_{tot} are given in nM, k_{off} is given in h⁻¹

Model II

This model was used to perform simulations to investigate the influence of K_D, target concentration (R_{tot}) and tissue distribution (k_{in}) on *in vivo* tissue selectivity. To this end, four different

simulations were performed for a k_{in} value of 8.6 h^{-1} (fast tissue distribution) and for a k_{in} value of 0.86 h^{-1} (slow tissue distribution). An overview of the variable parameter values can be found in Table 2. An overview of all other parameters can be found in Supplemental 1.

Model III

Simulations were performed for Rimonabant, Δ^8 tetrahydrocannabinol (Δ^8 THC) and CP-55940 in a minimal-PBPK-TMDD model (Figure 3). The K_D at the selected targets (CB1, mGlu5, TRPV1, and 5-HT1a) was predicted by a QSAR per target model trained on the complete pChEMBL dataset per target. A fast dissociation from the receptor was assumed for all compounds by setting the k_{off} value to 10 h^{-1} at all receptors. Simulations were performed for a time span of 7 days during which a dose was administered every 24 hours.

In order to investigate the influence of increasing drug-target affinity without a change in equilibrium selectivity, additional simulations were performed in which the ratio between the different K_D values for the different receptors was kept the same while adjusting the absolute K_D values by a factor 10 and 100. Simulations were performed for a time span of 7 days with dosing once every 24 hours. The dose was scaled for the K_D to obtain similar equilibrium occupancies in all simulations.

3 QSAR

A Random Forest QSAR per target model was developed using the Random Forest package from CRAN. [52]

3.1 Data selection

Bio-activity data from ChEMBL22 was used for the development of the QSAR model.[53] High quality data was selected by setting assay confidence at 9 and requiring an assigned pChEMBL value for all data points.[22] This means that a direct single protein target is assigned to the ligand. PubChem database data and potential duplicates were excluded from the dataset. Bioactivity data from ChEMBL was limited to four different constants: K_D , K_i , IC_{50} and EC_{50} . It has been shown previously that K_i and IC_{50} can be combined for modelling.[54] In order to check if these constants could be used interchangeably, a statistical analysis of their pChEMBL values was performed. In this analysis, the mean, standard deviation (SD), median and median absolute deviation (MAD) were analysed within and between all four constants. An overview of all results is provided in Supplemental 4. Since from this analysis it could be concluded that the deviation between pChEMBL values between K_D and K_i do not differ significantly from the deviation within the K_D dataset, both K_D and K_i values were used in the model development.

The molecular structure of the ligands was extracted from the molfile and physicochemical properties and FCFP_6 circular fingerprints were calculated in Pipeline Pilot.[55] The FCFP_6 fingerprints were then converted to 768 feature properties for use in model training. Selection was performed based on the relative frequency of substructures per target, where the optimal frequency was close to being present in 50% of the ligands.

The complete dataset was split into a training set (70%) and validation set (30%). This split was performed seven times, each time with a different seed (111, 222, ..., 777) in order to create seven different datasets. In this way, the model training and validation could be performed 7 times, allowing for reproducibility analysis of the model performance results.

3.2 Training

For each target, a Random Forest model consisting of 500 trees was trained using the seven different training sets. The models were trained on a predefined set of properties consisting of $\log(P)$, molecular weight, number of proton donors, number of proton acceptors, number of rotatable bonds,

number of atoms, number of rings, number of aromatic rings, molecular solubility, molecular surface area, molecular polar surface area and the 768 FCFP_6 fingerprint properties that describe the molecular structure in more detail.

3.3 Validation

The model performance was validated internally and externally using the corresponding validation dataset per seed, as described above. Internal validation was performed by an out-of-bag (OOB) estimate and presented as the average R^2 regression coefficient and the root-mean-squared error (RMSE). [56] The OOB estimate method uses subsamples from the training dataset to determine the mean prediction error of the RF model. The RMSE is a value that measures the average magnitude of the error and is presented by the same unit as the dependent variable, which in this case is the pChEMBL value ($-\log K_D/K_i$ in M). External validation was performed by a regression validation of the validation dataset against the predicted pChEMBL values. These results are also presented as the average R^2 regression coefficient and the RMSE.

Results

1. Model I

The simulations in Figure 4 show *in vivo* kinetic target selectivity in all simulations, due to a difference in the k_{off} value for target 1 and target 2. However, the extent of the observed selectivity is dependent on the K_D value and target concentration. Given that optimisation is often performed towards lower k_{off} values, the target at which k_{off} is 0.01 h^{-1} is considered as the desired therapeutic target. Initially, target selectivity for the off-target is observed, but this selectivity reverses to selectivity for the therapeutic target over time in all simulations, except in Figure 4b, where the K_D is low and the target concentration is high. As it would be unlikely in drug development to develop two drugs with a 1000-fold different binding kinetics but the same K_D value, we also performed these simulations with 100-fold different binding kinetics and 10-fold different K_D values as presented in supplemental 5. In these figures, the same trend is observed, although the residual selectivity is higher due to the difference in K_D values.

In summary, we observed that both a high target concentration and a low K_D value decrease the *in vivo* kinetic target selectivity.

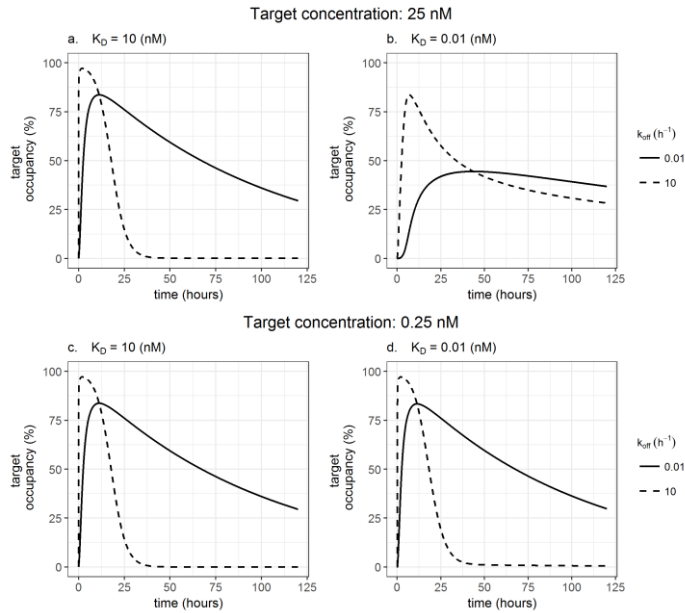


Figure 4. Target concentration and K_D determine the extent of *in vivo* kinetic target selectivity in Model I. Target selectivity is characterised by a difference in target occupancy between target 1 (solid) and target 2 (dashed). The parameter values for these simulations can be found in Supplemental 1.

2. Model II

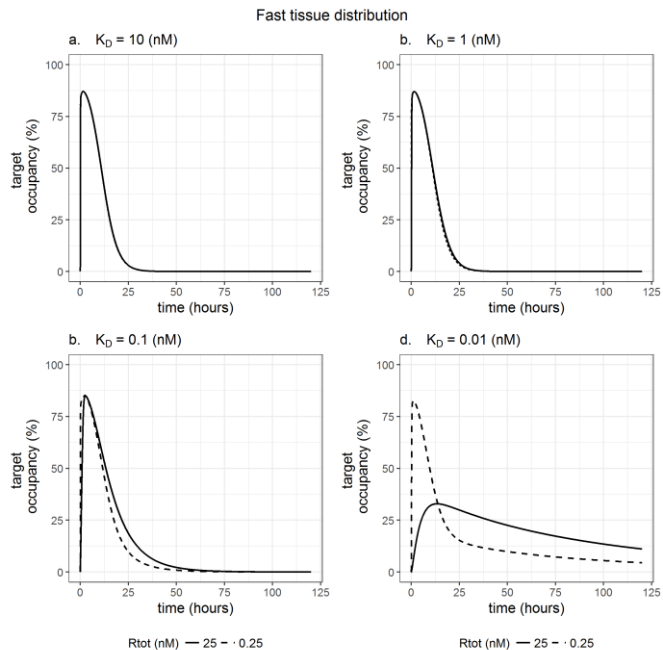


Figure 5. Tissue selectivity reverses to off-target selectivity as K_D decreases in Model II. k_{in} is 8.6 h^{-1} . Tissue selectivity is characterised by a difference in target occupancy between target 1 (solid) and target 2 (dashed). The parameter values for these simulations can be found in Supplemental 1.

For the simulations presented in Figure 5, no difference in k_{off} or K_D values between the two target sites could be included, since the ligand binds to the same target and the differences in target occupancy arise due to a difference in the target concentration. No selectivity is observed for the higher K_D values (10 and 1 nM), and only marginal selectivity is observed for lower K_D -values (0.1 nM and 0.01 nM). Assuming that the target concentration in the target tissue is higher than the target concentration in the off-target tissue, the lowest simulated K_D -values showed selectivity in the first 12 hours to the off-target tissue after which selectivity for the target tissue is observed (Figure 5d). Marginal selectivity for the target tissue is observed for a K_D value of 0.1 nM (Figure 5c). Taken together, this means that the K_D and receptor concentrations influence the extent of *in vivo* tissue selectivity.

The simulations in Figure 5 were performed for fast tissue distribution based on the reported blood flow of well-perfused organs in the human body.[37]

Figure 6 shows the simulation results for slower tissue distribution, representing limited perfusion of the target site (e.g. in a synaptic cleft) or the presence of diffusion barriers (e.g. for intracellular or CNS targets). In these figures, the same patterns are observed as for fast tissue distribution, but the observed selectivity is greater and the affinity for maximal selectivity for the target-rich tissue is lower.

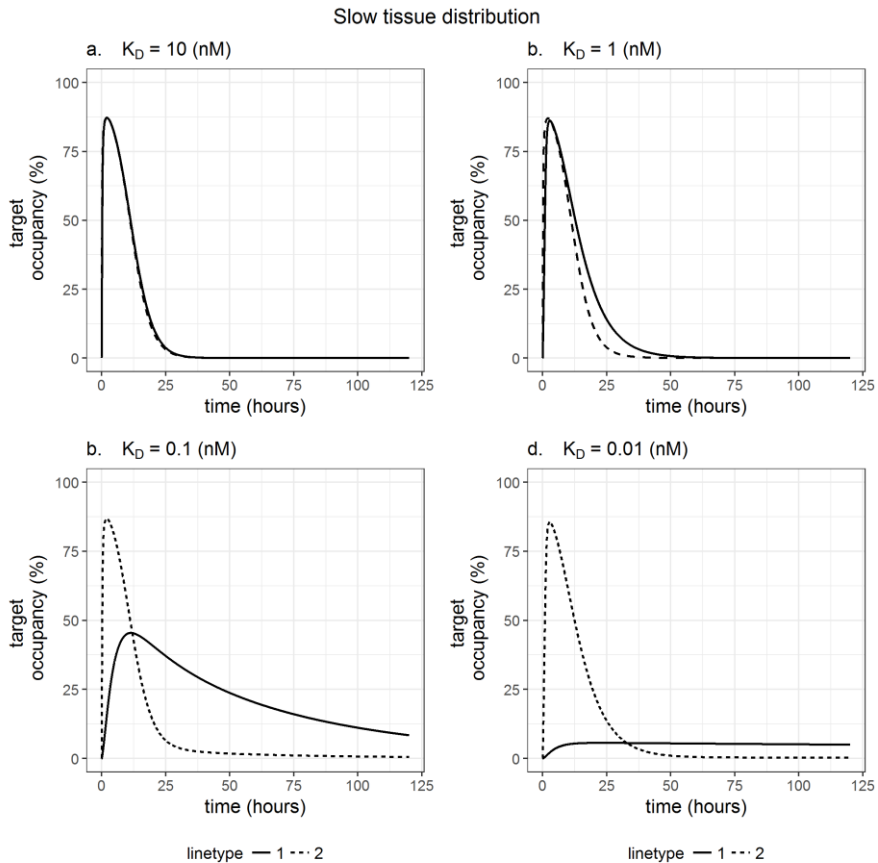


Figure 6. Slower tissue distribution amplifies the influence of K_D on tissue selectivity in Model II. k_{in} is 0.86 h^{-1} . Tissue selectivity is characterised by a difference in target occupancy between target 1 (solid) and target 2 (dashed). The parameter values can be found in Supplemental 1.

3 QSAR-RF

From the simulations described above, it follows that there is an optimal K_D for both tissue selectivity and target selectivity. To facilitate the optimisation of the K_D , we aimed to predict the K_D value from the molecular structure with predictive QSAR modelling. In this study, a QSAR-RF model was developed. The results of the internal and external validation are given in **Figure 7**. For the OOB validation, R^2 values range from 0.57 to 0.70, with an average of 0.63 (SD 0.04) and RMSE values range between 0.64 and 0.83 with an average of 0.69 (SD 0.05). For external regression validation, the R^2 values range from 0.50 to 0.73 with an average of 0.62 (SD 0.05) and RMSE values ranging between 0.9 and 0.64 with an average of 0.71 (SD 0.06). These values indicate good model performance, since the error in public data is around 0.44 for pK_i data. Moreover, based on this error it has been shown that the theoretical maximal achievable R^2 value then becomes 0.81 for the perfect model. [57–59] A full overview of the results is supplied in Supplemental 4.

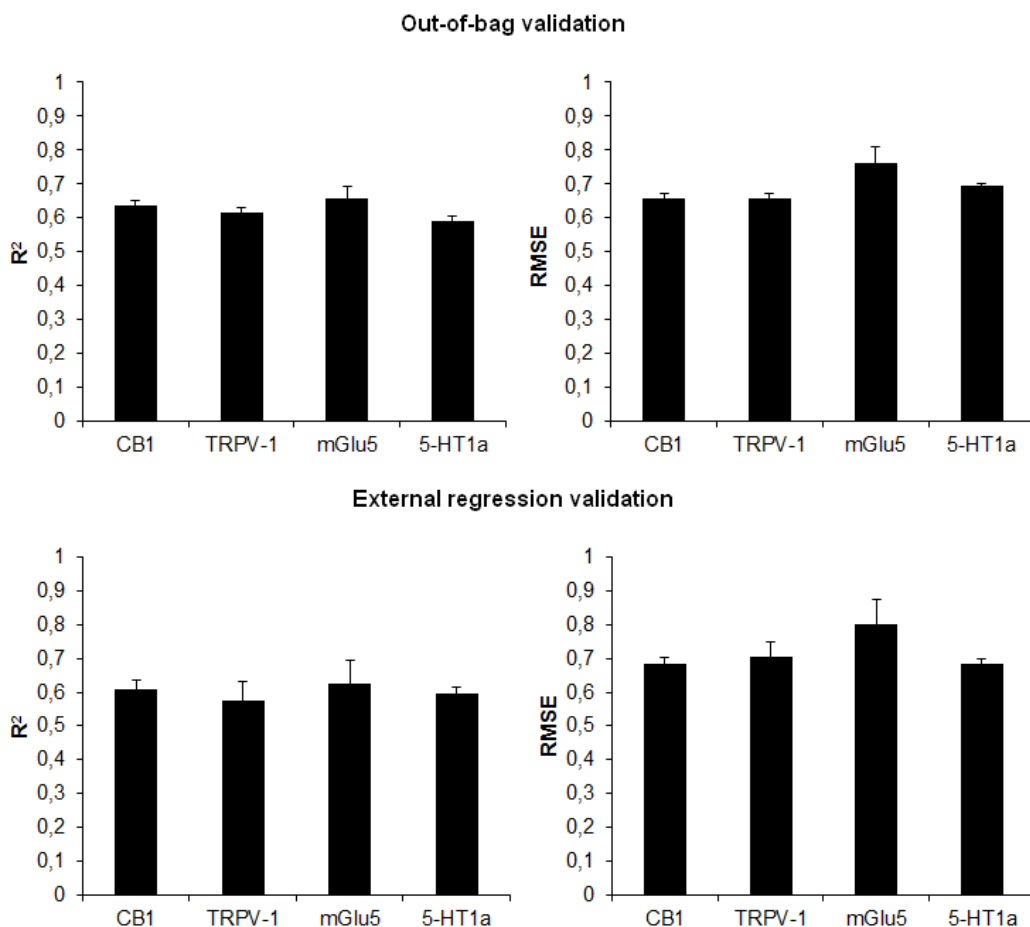


Figure 7. QSAR RF model performance regression validation. Internal out-of-bag validation resulted in an average R^2 value of 0.63 ± 0.06 (SD 0.04), with an RMSE of 0.69 ± 0.1 (SD 0.05). External regression validation gave an average R^2 value of 0.62 ± 0.12 (SD 0.05) with an RMSE of 0.71 ± 0.13 (SD 0.06).

4 Model III

To reflect a drug discovery/candidate selection scenario, the developed QSAR model was used to predict the affinity of the molecules Rimonabant, Δ^8 tetrahydrocannabinol (Δ^8 THC) and CP-55940 for the four selected receptors (CB1, TRPV1, mGlu5, 5-HT1a, **Figure 8**). These K_D values were then used to predict the selectivity over different brain regions (cerebellum, hypothalamus and the frontal cortex). The results of these simulations are given in **Figure 8**. For the target occupancy of Δ^8 THC, the compound with the lowest CB1

affinity, no selectivity is observed between brain regions. The target occupancy for the higher affinity compounds Rimonabant and CP-55940 show a slower increase of target occupancy in the brain regions with the highest target concentrations, the cerebellum and frontal cortex compared to the hypothalamus. The difference in target occupancy between the brain regions is similar for all targets, which results in a change in target selectivity across brain regions. Two days after the start of Rimonabant dosing, for example, the simulated target occupancy at TRPV1 in the hypothalamus is similar to the CB1 target occupancy in cerebellum and frontal cortex.

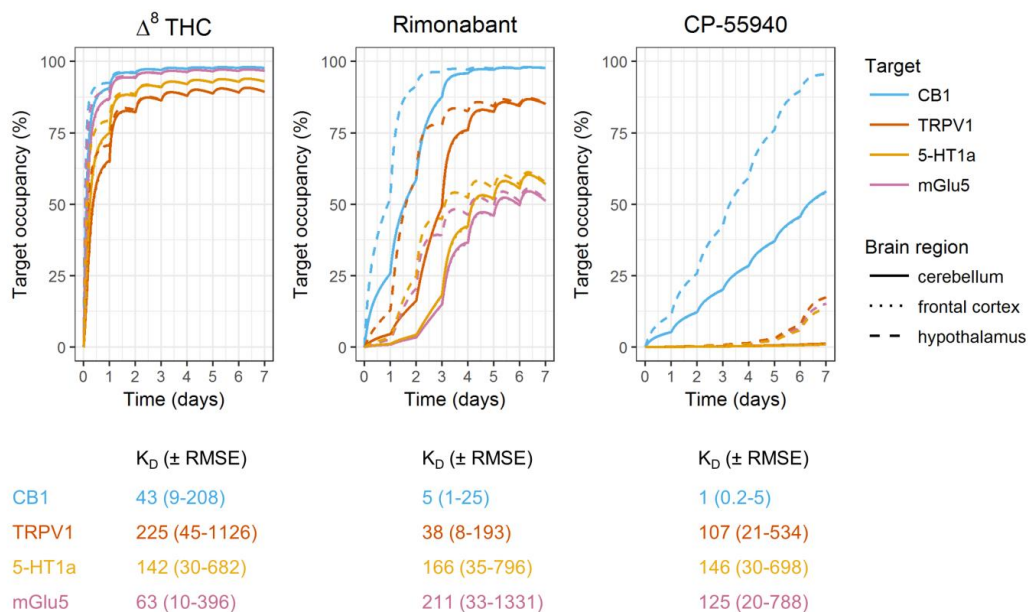


Figure 8. Simulated PK-profile for Rimonabant in cerebellum, frontal cortex and hypothalamus. Predicted K_D values of Δ^8 -THC, Rimonabant and CP-55940 at the CB1, 5-HT1a, mGlu5 and TRPV1 receptor were used in these simulations. k_{off} values were assumed to be 10 h^{-1} . A dose of 10^4 nM was administered every 24 hours. $R_{tot,cer,CB1} = 527 \text{ nM}$, $R_{tot,cer,mGlu5} = 5.1 \text{ nM}$, $R_{tot,cer,TRPV1} = 19 \text{ nM}$, $R_{tot,cer,5-HT1a} = 0.01$, $R_{tot,hyp,CB1} = 248 \text{ nM}$, $R_{tot,hyp,mGlu5} = 16 \text{ nM}$, $R_{tot,hyp,TRPV1} = 13 \text{ nM}$, $R_{tot,hyp,5-HT1a} = 2.37$, $R_{tot,fc,CB1} = 529 \text{ nM}$, $R_{tot,fc,mGlu5} = 25 \text{ nM}$, $R_{tot,fc,TRPV1} = 12 \text{ nM}$, $R_{tot,fc,5-HT1a} = 1.7$.

For CP-55940, it takes more than 7 days to reach the maximal occupancies in the cerebellum and frontal cortex, while this delay would be even more extensive for lower doses. It should be noted that equilibrium selectivity (i.e. the difference in K_D values for the different receptors) is different for the compounds in Figure 8. To obtain a better view of the role of the value of the K_D as such, rather than the K_D ratio between targets, the simulations for Rimonabant were repeated with the same K_D ratio between targets and tenfold increased and decreased K_D values, as shown in Supplemental 6, Figure I. Additionally, to explore the influence of error propagation from the QSAR model into model III, simulations were performed for the lowest and highest K_D value within the RMSE based $K_D(\pm)$ prediction range as shown in Supplemental 6, Figure II. Summarizing the results, it is consistently found that the selectivity profile changes drastically over time while this would not be expected based on plasma concentrations and K_D values alone.

Discussion

In this study, we have shown that the integration of target binding and PBPK modelling demonstrates the importance of target concentrations, target site distribution kinetics, the K_D and k_{off} for both *in vivo* target selectivity and tissue selectivity. We observe that a low K_D , in combination with a high target concentration, decreased the kinetic target selectivity. Moreover, we find that an increasing K_D can both increase and decrease tissue selectivity, dependent on the target concentration and tissue distribution. The demonstrated mechanistic modelling can thus be instrumental to find an optimal K_D value for a specific

target/therapeutic area. To utilize this approach most effectively, our QSAR model to predict CB1 and off-target K_D values can be used to predict tissue and target selectivity directly from the molecular structure. Using this combination of models, our simulations for the CB1 ligands confirm that lower K_D values for all targets can decrease the CB1 and brain region selectivity significantly during the first days of treatment.

Our results suggest that optimisation towards high drug-target affinity and slow drug-target dissociation, as is commonly performed within the current drug development paradigm, may not result in the most selective compounds. While this study demonstrates the influence of target concentrations on the target occupancy in different tissues, the influence of target concentrations on the occupancy-response relationship has previously been described as driving factor for tissue selectivity of partial agonists.[60–62] For the development of more selective drugs, target concentrations of both the intended target and off-targets as well as distribution to the target tissue/target site should be taken into consideration. In this respect, it is important to consider that distribution to the target site is not only dependent on distribution into the target tissue, but also on the localisation of the target within this tissue (e.g. in the blood stream or intracellularly). Moreover, factors such as target concentrations and tissue distribution may be altered in a disease state, which is important for the translation from healthy volunteers to patients.[24,63–65] Finally, it should be considered that there is an increased interest towards allosteric modulation in CNS drug discovery due to the potential benefits with regard to selectivity and side effects.[66] However, it has also been shown that allosteric modulators display different physicochemical and efficacy (K_i versus ligand efficacy) profiles compared to orthosteric ligands.[67] These parameters can be included in the modelling approach for future studies.

The methods described in this study provide valuable insights for drugs in later stages of the drug development process. The selectivity profiles in **Figure 8**, for example, would result in underestimation of CB1 selectivity in (pre)clinical studies, if only the first 7 days were studied. This might lead to the unnecessary discontinuation of the development of valuable drug candidates. Moreover, the slowly increasing target occupancy for high affinity drugs such as CP-55940 might lead to a clinically undesired delay and unfavourable selectivity between the initiation of treatment and the onset of the therapeutic effect. This can potentially be mitigated by a higher dose (i.e. a loading dose), which can be lowered as soon as steady state occupancy is reached. Since monitoring of occupancy levels in the clinic is hardly feasible, this would require in-depth knowledge of the mechanisms and predicted occupancy profile as described in this study. Moreover, it should be noted that the target occupancy will decline only slowly after discontinuation of treatment and that it might take several days or even weeks for these high affinity drugs before the target occupancy is back to insignificant levels. This could be counteracted in the clinic by administration of a competitive antagonist or agonist to displace the drug from the receptor and enhance the clearance out of the target binding tissue.

The simulations in this study were all based on physiological parameter values as obtained from PBPK models and target concentration literature. However, additional assumptions were sometimes necessary. For the simulations in Figure 6, the tissue distribution of the drug was not based on the blood flow through well-perfused organs, as for the other figures, but we assumed a delayed distribution due to, for example, limited diffusion into a synaptic cleft or the cytosol. The magnitude of this delay is compound and target specific and this assumption will thus only hold for a limited number of compounds. Secondly, the simulation in Figure 8 assumed fast binding kinetics as the actual binding kinetics of Rimonabant have been reported to be complex and therefore hard to accurately determine in *in vitro* studies.[68,69] The assumption of fast binding kinetics is supported by the short dissociation half-life as reported by Packeu *et al.*[70] Additionally, this assumption will be valid for any drug for which the binding kinetics are not rate-limiting compared to the pharmacokinetics, but slower binding kinetics could change the outcome of the simulations, as shown in Figure 4 and in previous studies. [5,6] Thirdly, a number of assumptions concerning (interspecies) translatability of target densities were made in order to obtain useful target densities for the simulations in Figure 8. In general, the quality of absolute tissue-specific target concentration data, rather than relative expression values, might be limited. This is illustrated by the large deviations between

experimental tissue density results found in the literature between PET-studies and tissue 'no wash' assay experiments. [41,71] Furthermore, the limited amount of information on target-site distribution for the simulations in Figure 8 limits the predictive value of these simulations. These simulations should therefore be considered as a prediction of the relevant parameters for combined target and tissue selectivity for a realistic set of target concentrations and K_D values, rather than a precise prediction of target occupancy values for the simulated CB1 ligands. One of the most striking findings in our study is that increasing the K_D in drug development can both increase and decrease the target and tissue selectivity. This demonstrates the relevance of target concentrations and tissue distribution, and the valuable role of mechanistic modeling.

The prediction error that is observed for the K_D predictions of the developed QSAR model introduces an extra level of uncertainty into the overall reliability of the selectivity predictions. The largest RMSE value in this study was found for the mGlu5 QSAR, with an average value of 0.8. This value relates to the deviation of the predictions from the actual pChEMBL value, and has the same unit as the dependent variable, which in this case is the $-\log K_D$. This uncertainty is therefore carried on into the pharmacological simulations. From the simulations performed with the highest and lowest value within the K_D prediction range of Rimonabant, it can be concluded that this propagation of error does influence the observed selectivity profile. This error is limited to the extent of selectivity and the distribution across brain regions during the first one to four days. However, part of this error is already present in the public data that was used to train our QSAR model, in which a larger standard deviation is found compared to the Rimonabant predictions at the CB1 receptor from the QSAR model (Supplemental 4, Figure I). Additionally, having the ability to predict the selectivity profile in the earliest stages of drug discovery justifies the use of predictions with significant uncertainty. Moreover, both the overrepresentation and underrepresentation of structural features or scaffolds in the ChEMBL database might decrease the predictive power for new compounds that do not share these structural features.

Although the predictive value of the presented models is limited by the assumptions we made, the presented insight into the influence of the target concentration and tissue distribution kinetics is in line with the previous analysis of more simple models with only one target and one tissue.[6] Moreover, the relevance of incorporating target binding in PBPK models for the accurate prediction of tissue concentrations has been demonstrated before.[13] The basic principle behind the role of the K_D and target concentration on the duration of occupancy is the high concentration of target-bound drug concentrations compared to unbound drug concentrations at the target site. This is mainly relevant for drugs with a high K_D and target concentration and at a target occupancy that is not completely saturated. If this target occupancy is increasing, drug-target association will deplete the unbound target site concentration, and if the occupancy is decreasing, drug-target dissociation will increase the unbound target site concentration compared to plasma concentrations.

In summary, the information presented in this study provides new insights into the mechanisms underlying *in vivo* target and tissue selectivity, specifically in relation to drug-target affinity, target concentration, tissue and target-site distribution, as well as binding kinetics. The study provides situations in which selectivity is expected to occur, which may aid as a lead towards creating ligands with the desired selectivity profile. Additionally, the demonstrated integration of mechanistic modelling and machine learning could enable the incorporation of these insights in the earliest phases of drug discovery. The need for this model-based selectivity optimisation is especially valuable for therapeutic areas in which an optimal target or tissue selectivity profile is difficult to obtain (e.g. in oncology) and might be less valuable for therapeutic areas where selectivity is less challenging and the traditional minimisation of the K_D is desired (e.g. for antibiotic/antiviral targets that are not expressed in human cells).

Conclusions

Simulations performed in semi-physiological pharmacological models with target binding revealed an important role for the target concentration and tissue distribution, next to the K_D and k_{off} values, in determining the extent of selectivity. Interestingly, it was observed that the optimal selectivity is not observed for the drug that displays the highest drug-target affinity when assuming that the desired target

concentrations are high and the desired binding kinetics are slow. Additionally, it was observed that kinetic selectivity is unlikely when the target concentrations and the drug-target affinity are high, while tissue selectivity is first increased and then decreased for increasing target concentrations and drug-target affinities. The context-dependent optimum of drug-target affinity in determining the extent of selectivity demonstrates the value of K_D prediction for drug development. Taken together, this study demonstrates the potential of integrative predictive modelling in providing improved strategies to optimize drug candidates for maximal *in vivo* selectivity.

Acknowledgements

The authors are part of the K4DD consortium, which is supported by the Innovative Medicines Initiative Joint Undertaking (IMI JU) under grant agreement no 115366. The IMI JU is a project supported by the EU's Seventh Framework Programme (FP7/2007–2013) and the European Federation of Pharmaceutical Industries and Associations (EFPIA).

References

1. Bowes J, Brown AJ, Hamon J, et al. Reducing safety-related drug attrition: the use of in vitro pharmacological profiling. *Nat Rev Drug Discov* 2012;11(12):909–22
2. Benson N, Metelkin E, Demin O, et al. A systems pharmacology perspective on the clinical development of Fatty Acid amide hydrolase inhibitors for pain. *CPT pharmacometrics Syst Pharmacol* 2014;3:e91
3. Yuraszck T, Kasichayanula S, Benjamin JE. Translation and Clinical Development of Bispecific T-cell Engaging Antibodies for Cancer Treatment. *Clin Pharmacol Ther* 2017;101(5):634–45
4. Copeland RA, Pompliano DL, Meek TD. Drug-target residence time and its implications for lead optimization. *Nat Rev Drug Discov* 2006;5(9):730–9
5. Dahl G, Akerud T. Pharmacokinetics and the drug-target residence time concept. *Drug Discov Today* 2013;18(15–16):697–707
6. de Witte WEA, Danhof M, van der Graaf PH, et al. In vivo Target Residence Time and Kinetic Selectivity: The Association Rate Constant as Determinant. *Trends Pharmacol Sci* 2016;37(10):831–42
7. Guo D, Dijksteel GS, Van Duijl T, et al. Equilibrium and kinetic selectivity profiling on the human adenosine receptors. *Biochem Pharmacol* 2016;105:34–41
8. Rostami-Hodjegan A. Physiologically based pharmacokinetics joined with in vitro-in vivo extrapolation of ADME: a marriage under the arch of systems pharmacology. *Clin Pharmacol Ther* 2012;92(1):50–61
9. Mager DE, Krzyzanski W. General Pharmacokinetic Model for Drugs Exhibiting Target-Mediated Drug Disposition. *Pharm Res* 2005;22(10):1589–96
10. Luu KT, Bergqvist S, Chen E, et al. A model-based approach to predicting the human pharmacokinetics of a monoclonal antibody exhibiting target-mediated drug disposition. *J Pharmacol Exp Ther* 2012;341(3):702–8
11. Zhang L, Mager DE. Physiologically-based pharmacokinetic modeling of target-mediated drug disposition of bortezomib in mice. *J Pharmacokinetic Pharmacodyn* 2015;42(5):541–52
12. Page KR, Mezzalana E, MacDonald AJ, et al. Temporal pharmacokinetic/pharmacodynamic interaction between human CD3ε antigen-targeted monoclonal antibody orelizumab and CD3ε binding and expression in human peripheral blood mononuclear cell static culture. *J Pharmacol Exp Ther* 2015;355(2):199–205
13. Plowchalk DR, Andersen ME, deBethizy JD. A physiologically based pharmacokinetic model for nicotine disposition in the Sprague-Dawley rat. *Toxicol Appl Pharmacol* 1992;116(2):177–88
14. Yang RSH, Thomas RS, Gustafson DL, et al. Approaches to developing alternative and predictive toxicology based on PBPK/PD and QSAR modeling. *Environ Health Perspect* 1998;106(6):1385–93
15. Knaak JB, Dary CC, Power F, et al. Physicochemical and Biological Data for the Development of Predictive Organophosphorus Pesticide QSARs and PBPK/PD Models for Human Risk Assessment. *Critical reviews in toxicology*. 2004. 143-207 p
16. Price K, Krishnan K. An integrated QSAR-PBPK modelling approach for predicting the inhalation toxicokinetics of mixtures of volatile organic chemicals in the rat. *SAR QSAR Environ Res* 2011;22(1–2):107–28
17. Van Der Graaf PH, Nilsson J, Van Schaick EA, et al. Multivariate quantitative structure-pharmacokinetic relationships (QSPKR) analysis of adenosine A1 receptor agonists in rat. *J Pharm Sci* 1999;88(3):306–12
18. Westen GJP Van, Hoven OO Van Den, Pijl R Van Der, et al. Identifying Novel Adenosine Receptor Ligands by Simultaneous Proteochemometric Modeling of Rat and Human Bioactivity Data. *J Med Chem* 2012;55:7010–20
19. Unterthiner T. Deep Learning as an Opportunity in Virtual Screening. *Workshop on Deep Learning and Representation Learning* 2014. p. 1–9
20. Christmann-Franck S, Van Westen GJP, Papadatos G, et al. Unprecedentedly Large-Scale Kinase Inhibitor Set Enabling the Accurate Prediction of Compound-Kinase Activities: A Way toward Selective Promiscuity by Design? *J Chem Inf Model* 2016;56(9):1654–75
21. Gaulton A, Bellis LJ, Bento AP, et al. ChEMBL: a large-scale bioactivity database for drug discovery. *Nucleic Acids Res* 2012;40(D1):D1100–7
22. Papadatos G, Gaulton A, Hersey A, et al. Activity, assay and target data curation and quality in the ChEMBL database. *J Comput Aided Mol Des* 2015;29(9):885–96
23. Mackie K. Cannabinoid receptors: Where they are and what they do. *J Neuroendocrinol* 2008;20(SUPPL. 1):10–4
24. Miller LKL, Devi L a. The highs and lows of cannabinoid receptor expression in disease: mechanisms and their therapeutic implications. *Pharmacol Rev* 2011;63(3):461–70
25. Pertwee RG, Howlett a C, Abood ME, et al. International Union of Basic and Clinical Pharmacology . LXXIX . Cannabinoid Receptors and Their Ligands : Beyond CB 1 and CB 2. *Pharmacol Rev* 2010;62(4):588–631
26. Bird MK, Lawrence AJ. The promiscuous mGlu5 receptor - a range of partners for therapeutic possibilities? *Trends Pharmacol Sci* 2009;30(12):617–23
27. Brotchie JM. CB1 cannabinoid receptor signalling in Parkinson's disease. *Curr Opin Pharmacol* 2003;3(1):54–61
28. Terzian ALB, Aguiar DC, Guimarães FS, et al. Modulation of anxiety-like behaviour by Transient Receptor Potential Vanilloid Type 1 (TRPV1) channels located in the dorsolateral periaqueductal gray. *Eur*

Neuropsychopharmacol 2009;19(3):188–95

29. Johnson K a, Conn PJ, Niswender CM. Glutamate receptors as therapeutic targets for Parkinson's disease. *CNS Neurol Disord Drug Targets* 2009;8(6):475–91
30. Team Rs. RStudio: Integrated Development Environment for R. Boston, MA; 2016.
31. R Core Team. R: A language and environment for statistical computing. R Found Stat Comput Vienna, Austria URL <http://wwwR-project.org/> 2013;
32. Dassault Systèmes BIOVIA Pipeline Pilot. San Diego; 2017.
33. Heinemann A, Wischhusen F, Püschel K, et al. Standard Liver Volume in the Caucasian Population. *Liver Transplant Surg* 1999;5(5):366–8
34. Lüders E, Steinmetz H, Jäncke L. Brain size and grey matter volume in the healthy human brain. *Neuroreport* 2002;13(17):2371–4
35. Llinas RR, Walton KD, Lang EJ. *Cerebellum. The Synaptic Organization of the Brain* 2004. p. "Cerebellum"
36. Petryszak R, Keays M, Tang YA, et al. Expression Atlas update — an integrated database of gene and protein expression in humans, animals and plants. *Nucleic Acids Res* 2016;44:746–52
37. Levitt DG, Schnider TW. Human physiologically based pharmacokinetic model for propofol. *BMC Anesthesiol* 2005;5(1):4
38. Makris N, Swaab DF, van der Kouwe A, et al. Volumetric Parcellation Methodology of the Human Hypothalamus in Neuroimaging: Normative Data and Sex Differences. *Neuroimage* 2013;69(April):1–10
39. Yamamoto Y, Väliälto PA, van den Berg D-J, et al. A Generic Multi-Compartmental CNS Distribution Model Structure for 9 Drugs Allows Prediction of Human Brain Target Site Concentrations. *Pharm Res* 2017;34(2):333–51
40. Breivogel CS, Sim LJ, Childers SR. Regional differences in cannabinoid receptor/G-protein coupling in rat brain. *J Pharmacol Exp Ther* 1997;282(3):1632–42
41. Patel S, Hamill TG, Connolly B, et al. Species differences in mGluR5 binding sites in mammalian central nervous system determined using in vitro binding with [¹⁸F]F-PEB. *Nucl Med Biol* 2007;34(8):1009–17
42. Han P, Korepanova A V., Vos MH, et al. Quantification of TRPV1 protein levels in rat tissues to understand its physiological roles. *J Mol Neurosci* 2013;50(1):23–32
43. Costes N, Merlet I, Zimmer L, et al. Modeling [¹⁸F]MPPF Positron Emission Tomography Kinetics for the Determination of 5-Hydroxytryptamine(1A) Receptor Concentration With Multiinjection. *J Cereb Blood Flow Metab* 2002;22(6):753–65
44. Glass M, Faull RLM, Dragunow M. Cannabinoid receptors in the human brain: a detailed anatomical and quantitative autoradiographic study on the fetal, neonatal and adult human brain. *Neuroscience* 1997;77(2):299–318
45. Liu P, Hamill TG, Chioda M, et al. Discovery of MK-3168: A PET tracer for imaging brain fatty acid amide hydrolase. *ACS Med Chem Lett* 2013;4(6):509–13
46. Szabo T, Biro T, Gonzalez AF, et al. Pharmacological characterization of vanilloid receptor located in the brain. *Mol Brain Res* 2002;98(1–2):51–7
47. Albe K, Butler MH, Wright B. Cellular concentrations of enzymes and their substrates. *J Theor Biol* 1990;143(2):163–95
48. Undén A, Tatemoto K, Mutt V, et al. Neuropeptide Y receptor in the rat brain. *Eur J Biochem* 1984;145(3):525–30
49. Milo R. What is the total number of protein molecules per cell volume? A call to rethink some published values. *Bioessays* 2013;35(12):1050–5
50. Poulin P, Theil FP. A priori prediction of tissue: Plasma partition coefficients of drugs to facilitate the use of physiologically-based pharmacokinetic models in drug discovery. *J Pharm Sci* 2000;89(1):16–35
51. Ghose AK, Viswanadhan VN, Wendoloski JJ. Prediction of Hydrophobic (Lipophilic) Properties of Small Organic Molecules Using Fragmental Methods: An Analysis of ALOGP and CLOGP Methods. *J Phys Chem A* 1998;5639(98):3762–72
52. Hornik K. The Comprehensive R Archiv Network. *WIREs Comput Stat* 2012;4:394–8
53. Bento AP, Gaulton A, Hersey A, et al. The ChEMBL bioactivity database: an update. *Nucleic Acids Res* 2014;42(D1):D1083–90
54. Kalliokoski T, Kramer C, Vulpetti A, et al. Comparability of Mixed IC 50 Data – A Statistical Analysis. *PLoS One* 2013;8(4)
55. Rogers D, Hahn M. Extended-Connectivity Fingerprints. *J Chem Informatics Model* 2010;50:742–54
56. Sventnik V, Liaw A, Tong C, et al. Random forest: a tool for classification and regression in compound classification and QSAR modeling. *J Chem Inf Comput Sci* 2003;43(6):1947–58
57. Golbraikh A, Tropsha A. Beware of q²! *J Mol Graph Model* 2002;20(4):269–76
58. Tropsha A, Gramatica P, Gombar V. The Importance of Being Earnest: Validation is the Absolute Essential for Successful Application and Interpretation of QSPR Models. *QSAR Comb Sci* 2003;22(1):69–77
59. Kramer C, Kalliokoski T, Geddeck P, et al. The Experimental Uncertainty of Heterogeneous Public Ki Data. *J Med Chem* 2012;55:5165–73

60. Yassen A, Olofsen E, Romberg R, et al. Mechanism-based PK/PD modeling of the respiratory depressant effect of buprenorphine and fentanyl in healthy volunteers. *Clin Pharmacol Ther* 2007;81(1):50–8
61. Schaick EA Van, Tukker HE, Roelen HCPF, et al. Selectivity of action of 8-alkylamino analogues of N6-cyclopentyladenosine in vivo: haemodynamic versus anti-lipolytic responses in rats. *Br J Pharmacol* 1998;124:607–18
62. van der Graaf PH, Schaick EA Van, Visser SAG, et al. Mechanism-Based Pharmacokinetic-Pharmacodynamic Modeling of Antilipolytic Effects of Adenosine A 1 Receptor Agonists in Rats : Prediction of Tissue-Dependent Efficacy. *J Pharmacol* 1999;290(2):702–9
63. Walawalkar YD, Vaidya Y, Nayak V. Alteration in transforming growth factor- β receptor expression in gallbladder disease: implications of chronic cholelithiasis and chronic Salmonella typhi infection. *Gastroenterol Insights* 2016;7(1):39–42
64. Epling-burnette PK, Painter JS, Chaurasia P, et al. Dysregulated NK receptor expression in patients with lymphoproliferative disease of granular lymphocytes Dysregulated NK receptor expression in patients with lymphoproliferative disease of granular lymphocytes. *Blood* 2011;103(9):3431–9
65. Atkinson H, England JA, Rafferty A, et al. Somatostatin receptor expression in thyroid disease. *Int J Exp Pathol* 2013;94(3):226–9
66. Conn PJ, Christopoulos A, Lindsley CW. Allosteric modulators of GPCRs: a novel approach for the treatment of CNS disorders. *Nat Rev drug Discov* 2010;8(1):41–54
67. Westen GJP Van, Gaulton A, Overington JP. Chemical, Target, and Bioactive Properties of Allosteric Modulation. *PLoS Comput Biol* 2014;10(4)
68. Wennerberg M, Balendran A, Clapham JC, et al. Unravelling the complex dissociation of [3H]-rimonabant from plated CB1 cannabinoid receptor-expressing cells. *Fundam & Clinical Pharmacol* 2010;24:181–7
69. Wennerberg M, Cheng L, Hjorth S, et al. Binding properties of antagonists to Cannabinoid receptors in intact cells. *Fundam Clin Pharmacol* 2011;25:200–10
70. Packeu A, Wennerberg M, Balendran A, et al. Estimation of the dissociation rate of unlabelled ligand-receptor complexes by a “two-step” competition binding approach. *Br J Pharmacol* 2010;161(6):1311–28
71. Kågedal M, Cselényi Z, Nyberg S, et al. Non-linear mixed effects modelling of positron emission tomography data for simultaneous estimation of radioligand kinetics and occupancy in healthy volunteers. *Neuroimage* 2012;61(4):849–56
72. Kennedy DN, Lange N, Makris N, et al. Gyri of the Human Neocortex : An MRI-based Analysis of Volume and Variance. *Cereb cortex* 1998;8(4):372–84

Supplemental 1

A. Model I

$$\frac{dac}{dt} = -ack_a$$

$$\frac{dbl}{dt} = ack_a + k_{outbt}bt + k_{outnbt}nbt + k_{outli}li - bl(k_{inbt} + k_{innbt} + k_{inli})$$

$$\frac{dbt}{dt} = k_{inbt}bl - k_{outbt}bt - k_{on1}bt \left(Rtot1 - \frac{RL1}{V_{bt}} \right) + k_{off1}RL1 - k_{on2}bt \left(Rtot2 - \frac{RL2}{V_{bt}} \right) + k_{off2}$$

$$\frac{dnbt}{dt} = k_{innbt}bl - k_{outnbt}nbt$$

$$\frac{dli}{dt} = k_{inli}bl - k_{outli}li - kFli$$

$$\frac{dRL1}{dt} = k_{on1}bt \left(Rtot1 - \frac{RL1}{V_{bt}} \right) - k_{off1}RL1$$

$$\frac{dRL2}{dt} = k_{on2}bt \left(Rtot2 - \frac{RL2}{V_{bt}} \right) - k_{off2}RL2$$

Table S1. Input parameters for model I. k_{in} is the inwards distribution rate constant, V is volume, kF is the forward rate of elimination constant, k_a is the absorption rate constant, bt is binding tissue, nbt is nonbinding tissue, li is liver, bl is blood.

Parameter	Value	Unit
k_{inbt}	8.6	h^{-1}
k_{innbt}	25	h^{-1}
k_{inli}	27	h^{-1}
V_{bl}	5.5	L
V_{bt}	1.4	L
V_{nbt}	61	L
V_{li}	1.8	L
kF	100	h^{-1}
k_a	0.25	h^{-1}

B. Model II

$$\frac{dac}{dt} = -ack_a$$

$$\frac{dbl}{dt} = ack_a + k_{outbt}bt + k_{outnbt}nbt + k_{outli}li - bl(k_{inbt1} + k_{inbt2} + k_{innbt} + k_{inli})$$

$$\frac{dbt1}{dt} = k_{inbt1}bl - k_{outbt1}bt - k_{on}bt1 \left(Rtot1 - \frac{RL1}{V_{bt1}} \right) + k_{off}RL1$$

$$\frac{dbt2}{dt} = k_{inbt2}bl - k_{outbt2}bt - k_{on}bt2 \left(Rtot2 - \frac{RL2}{V_{bt2}} \right) + k_{off}RL2$$

$$\frac{dnbt}{dt} = k_{innbt}bl - k_{outnbt}nbt$$

$$\frac{dli}{dt} = k_{inli}li - k_{outli}li - kFli$$

$$\frac{dRL1}{dt} = k_{on}bt1 \left(Rtot1 - \frac{RL1}{V_{bt1}} \right) - k_{off}RL1$$

$$\frac{dRL2}{dt} = k_{on}bt2 \left(Rtot2 - \frac{RL2}{V_{bt2}} \right) - k_{off}RL2$$

i. Fast distribution

Table S2. Input parameters for the fast distribution simulations in model II. k_{in} is the inwards distribution rate constant, V is volume, k_F is the forward rate of elimination constant, k_a is the absorption rate constant, bt is binding tissue, nbt is nonbinding tissue, li is liver, bl is blood, R_{tot} is receptor concentration, k_{on} is the ligand-target association rate constant.

Parameter	Value	Unit
k_{inbt1}	8.6	h^{-1}
k_{inbt2}	8.6	h^{-1}
k_{innbt}	17	h^{-1}
k_{inli}	27	h^{-1}
V_{bl}	5.5	L
V_{bt1}	1.4	L
V_{bt2}	1.4	L
V_{nbt}	60	L
V_{li}	1.8	L
k_F	100	h^{-1}
R_{tot1}	25	nM
R_{tot2}	0.25	nM
k_{off}	10	$nM^{-1}h^{-1}$

ii. Slow distribution

Table S3. Input parameters for the slow distribution simulations in model II. k_{in} is the inwards distribution rate constant, V is volume, k_F is the forward rate of elimination constant, k_a is the absorption rate constant, bt is binding tissue, nbt is nonbinding tissue, li is liver, bl is blood, R_{tot} is receptor concentration, k_{on} is the ligand-target association rate constant.

Parameter	Value	Unit
k_{inbt1}	8.6	h^{-1}
k_{inbt2}	8.6	h^{-1}
k_{innbt}	17	h^{-1}
k_{inli}	27	h^{-1}
V_{bl}	5.5	L
V_{bt1}	1.4	L
V_{bt2}	1.4	L
V_{nbt}	60	L
V_{li}	1.8	L
k_F	100	h^{-1}
R_{tot1}	25	nM
R_{tot2}	0.25	nM
k_{off}	10	$nM^{-1}h^{-1}$

C. Model III

$$\frac{dac}{dt} = -ack_a$$

$$\frac{dbl}{dt} = ack_a + Q_{cer} \frac{cer/V_{cer}}{P_{cer}} + Q_{fc} \frac{fc/V_{fc}}{P_{fc}} + Q_{hyp} \frac{hyp/V_{hyp}}{P_{hyp}} Q_{cer} + \frac{nbt/V_{nbt}}{P_{nbt}} + Q_{li} \frac{li/V_{li}}{P_{li}} - Q_{bl} \frac{bl}{V_{bl}}$$

$$\frac{dnbt}{dt} = Q_{nbt} \left(\frac{bl}{V_{bl}} - \frac{nbt/V_{nbt}}{P_{nbt}} \right)$$

$$\begin{aligned} \frac{dcer}{dt} = & Q_{cel} \left(\frac{bl}{V_{bl}} - \frac{cer/V_{cer}}{P_{cer}} \right) - k_{onCB1cer} \left(CB1_{cer} - \frac{CB1RL_{cer}}{V_{cer}} \right) + k_{offCB1} CB1RL_{cer} - k_{onmGlu5cer} \left(mGlu5_{cer} - \right. \\ & \left. \frac{mGlu5RL_{cer}}{V_{cer}} \right) + k_{offmGlu5} mGlu5RL_{cer} - k_{onTRPV1cer} \left(TRPV1_{cer} - \frac{TRPV1RL_{cer}}{V_{cer}} \right) + k_{offTRPV1} TRPV1RL_{cer} - \\ & k_{onHT1acer} \left(HT1a_{cer} - \frac{HT1aRL_{cer}}{V_{cer}} \right) + k_{offHT1a} HT1aRL_{cer} \end{aligned}$$

$$\begin{aligned} \frac{dhyp}{dt} = & Q_{hyp} \left(\frac{bl}{V_{bl}} - \frac{hyp/V_{hyp}}{P_{hyp}} \right) - k_{onCB1hyp} \left(CB1_{hyp} - \frac{CB1RL_{hyp}}{V_{hyp}} \right) + k_{offCB1} CB1RL_{hyp} - k_{onmGlu5hyp} \left(mGlu5_{hyp} - \right. \\ & \left. \frac{mGlu5RL_{hyp}}{V_{hyp}} \right) + k_{offmGlu5} mGlu5RL_{hyp} - k_{onTRPV1hyp} \left(TRPV1_{hyp} - \frac{TRPV1RL_{hyp}}{V_{hyp}} \right) + k_{offTRPV1} TRPV1RL_{hyp} - \\ & k_{onHT1ahyp} \left(HT1a_{hyp} - \frac{HT1aRL_{hyp}}{V_{hyp}} \right) + k_{offHT1a} HT1aRL_{hyp} \end{aligned}$$

$$\begin{aligned} \frac{dfc}{dt} = & Q_{fc} \left(\frac{bl}{V_{bl}} - \frac{fc/V_{fc}}{P_{fc}} \right) - k_{onCB1fc} \left(CB1_{fc} - \frac{CB1RL_{fc}}{V_{fc}} \right) + k_{offCB1} CB1RL_{fc} - k_{onmGlu5fc} \left(mGlu5_{fc} - \frac{mGlu5RL_{fc}}{V_{fc}} \right) + \\ & k_{offmGlu5} mGlu5RL_{fc} - k_{onTRPV1fc} \left(TRPV1_{fc} - \frac{TRPV1RL_{fc}}{V_{fc}} \right) + k_{offTRPV1} TRPV1RL_{fc} - k_{onHT1afc} \left(HT1a_{fc} - \right. \\ & \left. \frac{HT1aRL_{fc}}{V_{fc}} \right) + k_{offHT1a} HT1aRL_{fc} \end{aligned}$$

$$\frac{dli}{dt} = k_{inli} li - k_{outli} li - kFli$$

$$\frac{dCB1RL_{cer}}{dt} = k_{onCB1cer} \left(CB1_{cer} - \frac{CB1RL_{cer}}{V_{cer}} \right) - k_{offCB1} CB1RL_{cer}$$

$$\frac{dmGlu5RL_{cer}}{dt} = k_{onmGlu5cer} \left(mGlu5_{cer} - \frac{mGlu5RL_{cer}}{V_{cer}} \right) - k_{offmGlu5} mGlu5RL_{cer}$$

$$\frac{dTRPV1RL_{cer}}{dt} = k_{onTRPV1cer} \left(TRPV1_{cer} - \frac{TRPV1RL_{cer}}{V_{cer}} \right) - k_{offTRPV1} TRPV1RL_{cer}$$

$$\frac{dHT1aRL_{cer}}{dt} = k_{onHT1acer} \left(HT1a_{cer} - \frac{HT1aRL_{cer}}{V_{cer}} \right) - k_{offHT1a} HT1aRL_{cer}$$

$$\frac{dCB1RL_{hyp}}{dt} = k_{onCB1hyp} \left(CB1_{hyp} - \frac{CB1RL_{hyp}}{V_{hyp}} \right) - k_{offCB1} CB1RL_{hyp}$$

$$\frac{dmGlu5RL_{hyp}}{dt} = k_{onmGlu5hyp} \left(mGlu5_{hyp} - \frac{mGlu5RL_{hyp}}{V_{hyp}} \right) - k_{offmGlu5} mGlu5RL_{hyp}$$

$$\frac{dTRPV1RL_{hyp}}{dt} = k_{onTRPV1hyp} \left(TRPV1_{hyp} - \frac{TRPV1RL_{hyp}}{V_{hyp}} \right) - k_{offTRPV1} TRPV1RL_{hyp}$$

$$\frac{dHT1aRL_{hyp}}{dt} = k_{onHT1ahyp} \left(HT1a_{hyp} - \frac{HT1aRL_{hyp}}{V_{hyp}} \right) - k_{offHT1a} HT1aRL_{hyp}$$

$$\frac{dCB1RL_{fc}}{dt} = k_{onCB1fc} \left(CB1_{fc} - \frac{CB1RL_{fc}}{V_{fc}} \right) - k_{offCB1} CB1RL_{fc}$$

$$\frac{dmGlu5RL_{fc}}{dt} = k_{onmGlu5fc} \left(mGlu5_{fc} - \frac{mGlu5RL_{fc}}{V_{fc}} \right) - k_{offmGlu5} mGlu5RL_{fc}$$

$$\frac{dTRPV1RL_{fc}}{dt} = k_{onTRPV1fc} \left(TRPV1_{fc} - \frac{TRPV1RL_{fc}}{V_{fc}} \right) - k_{offTRPV1} TRPV1RL_{fc}$$

$$\frac{dHT1aRL_{fc}}{dt} = k_{onHT1afc} \left(HT1a_{fc} - \frac{HT1aRL_{fc}}{V_{fc}} \right) - k_{offHT1a} HT1aRL_{fc}$$

The clearances from brain extra-cellular fluid to the cerebrospinal fluid presented by Yamamoto *et al* are 0.0556, 0.0250, 0.0598, 0.0200, 0.0248, 0.0133, 0.0237, 0.0176 and 0.0254 ml/min, resulting in a mean value of 0.0295 ml/min. These values were allometrically scaled to humans by multiplying this value by $(70/0.25)^{0.75}$, resulting in a value of 2.02 ml/min, which equals to 0.121 L/h. In this study, the ECF volume in humans was reported as 0.240 L. Given that the equation for clearance is $CL = V * k_{out}$, k_{out} can be

calculated as $0.121 \text{ (L/h)}/0.240 \text{ (L)}$, resulting in a value of 0.504 h^{-1} . By multiplying this value by the tissue volume, the effective flow through the target site (cerebellum, hypothalamus, frontal cortex) is obtained.

Table S4. Model parameters for model III. Q is blood flow, P is the partition coefficient, V is volume, k_{off} is the ligand-target dissociation rate constant, kF is the forward rate of elimination constant, k_a is the absorption rate constant, bl is blood, nbt is nonbinding tissue, cer is cerebellum, hyp is hypothalamus, fc is frontal cortex, li is liver.

Parameter	Value	Unit	References
Qbl	335	L/h	[37]
Qnbt	$335 - 0.504 * (V_{\text{cer}} + V_{\text{hyp}} + V_{\text{fc}}) - 108$	L/h	
Qcer	$V_{\text{cer}} * 0.504$	L/h	[39]
Qhyp	$V_{\text{hyp}} * 0.504$	L/h	[39]
Qfc	$V_{\text{fc}} * 0.504$	L/h	[39]
Qli	27	L/h	[37]
Pnbt	46		
Pcer	13		
Phyp	13		
Pfc	13		
Pli	9.4		
Vbl	5.5	L	[37]
Vnbt	62	L	[37]
Vcer	0.15	L	[35]
Vhyp	$1.4 * 10^{-2}$	L	[38]
Vfc	0.27	L	[72]
Vli	1.8	L	[37]
k_{off}	10	h^{-1}	
kF	100	h^{-1}	
k_a	0.25	h^{-1}	
Dose	$5.0 * 10^4$	nM	

Supplemental 2

Table S5. Receptor density values obtained from literature. CB1 is cannabinoid 1 receptor, TRPV1 is vanilloid 1 receptor, 5-HT1a is serotonin 1a receptor, mGlu5 is metabotropic glutamate receptor 5. All these values are obtained from rat studies, unless otherwise specified

	CB1	CB1 ^a	mGlu5 ^b	TRPV1	TRPV1 ^c	5-HT1a ^b
	Bmax (pmol/mg protein)	Bmax (nM)	Bmax (nM)	Protein level (ng/mg lysate)	Protein level (nM)	Bmax (nM)
cerebellum	5.27	527	5.1	4.03	19	0.01 ^d
(frontal) cortex	5.29	529	25	2.53	12	1.70
hypothalamus	2.48	248	16 ^e	2.76	13	2.37 ^f
References	[40]		[41]	[42]		[43]

^a Conversion from pmol/mg protein to nM was obtained by multiplying with an assumed protein concentration of 100 mg/ml tissue.[48]

^b Values from humans.

^c These values were obtained by multiplying the protein level in ng/mg lysate with the ratio of protein level in pmol/mg protein[46] and in ng/mg lysate[42] and subsequent multiplication with an assumed protein concentration of 100 mg/ml tissue.[48]

^d This value was too low to be identified in the reference and was therefore set to a low concentration.

^e The Bmax value was calculated as the average of the cortex, caudate-putamen and cerebellum.

^f The reported value for the limbic average was used for the hypothalamus.

Supplemental 3

A. Physicochemical Properties

Table S6. Physicochemical properties for the partition coefficient calculations in the Integrated QSAR-RF PBPK-TMDD model. P is the octanol-water partition coefficient, Sw is the solubility in water, So is the solubility in octanol.

Ligand	logP	logSw	P	Sw	So
Δ^8 -THC	6.109	-6,152	$12 \cdot 10^5$	$7.05 \cdot 10^{-7}$	0.91
Rimonabant	6.613	-8,112	$41 \cdot 10^5$	$7.73 \cdot 10^{-9}$	0.03
CP-55940	6.162	-7,244	$14 \cdot 10^5$	$5.70 \cdot 10^{-8}$	0.08

B. Volume Fractions

Table S7. Volume fractions of water, neutral lipids and phospholipids in human tissues. Nbt is nonbinding tissue.

	Water	Neutral lipid	Phospholipid
Blood	0.8	0.0044	0.0021
Liver	0.72	0.039	0.028
Nbt	0.56	0.21	0.071
Brain	0.79	0.0462	0.0638

Supplemental 4

A. Compare Binding

i. Within

Table S8. Statistical analysis of the pChEMBL value deviations within measurements of the same bioactivity value and all bioactivity values together. Mean Δ is the mean difference between measurements of the same ligand at the same target. K_D is the dissociation rate constant, K_i is the inhibitory constant, IC_{50} is the half-maximal inhibitory constant ions, and EC_{50} is the half-maximal effective concentration.

	$K_D - K_D$	$K_i - K_i$	$IC_{50} - IC_{50}$	$EC_{50} - EC_{50}$	Any - Any
Mean Δ	0.32	0.44	0.61	0.50	0.61
Mean pChEMBL value	6.56 ± 0.14	7.29 ± 0.20	6.83 ± 0.29	6.74 ± 0.23	6.90 ± 0.28

ii. Between

Table S9. Statistical analysis of the pChEMBL value deviations between measurements of different bioactivity values. Mean Δ is the mean difference between measurements of the same ligand at the same target. K_D is the dissociation rate constant, K_i is the inhibitory constant, IC_{50} is the half-maximal inhibitory constant ions, and EC_{50} is the half-maximal effective concentration

	$K_D - K_i$	$K_i - IC_{50}$	$K_i - EC_{50}$	$IC_{50} - EC_{50}$
Mean Δ	0.16	0.50	0.52	0.21
Mean pChEMBL value	7.16 ± 0.19	6.93 ± 0.28	7.21 ± 0.23	6.83 0.29

B. Out-of-bag validation

i. R^2

Table S10. The R^2 values of the out-of-bag validation of the QSAR-RF model trained on seven different datasets. The R^2 values are reported per training of the model on a data set obtained using a different split seed.

Seed	CB1	TRPV1	ADORA2a	mGlu5	5-HT1a
111	0.62	0.61	0.67	0.59	0.62
222	0.64	0.59	0.67	0.67	0.57
333	0.65	0.61	0.68	0.70	0.59
444	0.66	0.63	0.66	0.63	0.58
555	0.64	0.64	0.68	0.68	0.58
666	0.62	0.62	0.67	0.67	0.59
777	0.63	0.61	0.68	0.64	0.59
STDEV	0.016	0.015	0.0076	0.038	0.015
AVG	0.64	0.62	0.67	0.65	0.59

ii. RMSE

Table S11. The RMSE values of the out-of-bag validation of the QSAR-RF model trained on seven different datasets. The root-mean squared error (RMSE) values are reported per training of the model on a dataset obtained using a different split seed.

Seed	CB1	TRPV1	ADORA2a	mGlu5	5-HT1a
111	0.67	0.66	0.67	0.83	0.68
222	0.66	0.68	0.67	0.69	0.70
333	0.65	0.67	0.67	0.73	0.70
444	0.64	0.66	0.68	0.81	0.70
555	0.65	0.65	0.66	0.76	0.70
666	0.67	0.64	0.67	0.77	0.69
777	0.66	0.67	0.66	0.75	0.69
STDEV	0.013	0.013	0.0076	0.047	0.0085
AVG	0.66	0.66	0.67	0.76	0.69

External Validation

i. R^2

Table S12. The R^2 values of external validation of the QSAR-RF model trained on seven different datasets. The R^2 values are reported per training of the model on a dataset obtained using a different split seed. The external validation was performed as a regression validation, using a validation dataset, containing only data which was not exposed to the model before validation.

	CB1	TRPV1	ADORA2a	mGlu5	5-HT1a
111	0.65	0.66	0.70	0.73	0.57
222	0.59	0.60	0.72	0.62	0.62
333	0.57	0.63	0.64	0.52	0.61
444	0.59	0.50	0.68	0.68	0.60
555	0.60	0.52	0.63	0.58	0.61
666	0.63	0.56	0.67	0.62	0.57
777	0.62	0.5	0.69	0.65	0.58
STDEV	0.028	0.056	0.031	0.070	0.020
AVG	0.61	0.58	0.68	0.63	0.60

ii. RMSE

Table S13. The RMSE values of the out-of-bag validation of the QSAR-RF model trained on seven different datasets. The root-mean squared error (RMSE) values are reported per training of the model on a dataset obtained using a different split seed. The external validation was performed as a regression validation, using a validation dataset, containing only data which was not exposed to the model before validation.

	CB1	TRPV1	ADORA2a	mGlu5	5-HT1a
111	0.66	0.64	0.65	0.72	0.68
222	0.68	0.70	0.64	0.75	0.66
333	0.7	0.66	0.69	0.90	0.67
444	0.71	0.74	0.64	0.74	0.69
555	0.70	0.73	0.70	0.85	0.69
666	0.67	0.76	0.67	0.79	0.69
777	0.67	0.68	0.66	0.87	0.7
STDEV	0.019	0.045	0.021	0.071	0.015
AVG	0.68	0.70	0.66	0.80	0.68

C. Prediction errors for Rimonabant at the CB1 receptor

In Figure S1, it can be seen that all predicted pChEMBL values for Rimonabant at the CB1 receptor fall within the confidence interval of pChEMBL values which are reported in the ChEMBL database. Although the structure of Rimonabant was present in the training set, this is indicative of a reliable prediction of the K_D values (at the CB1 receptor) used in this study.

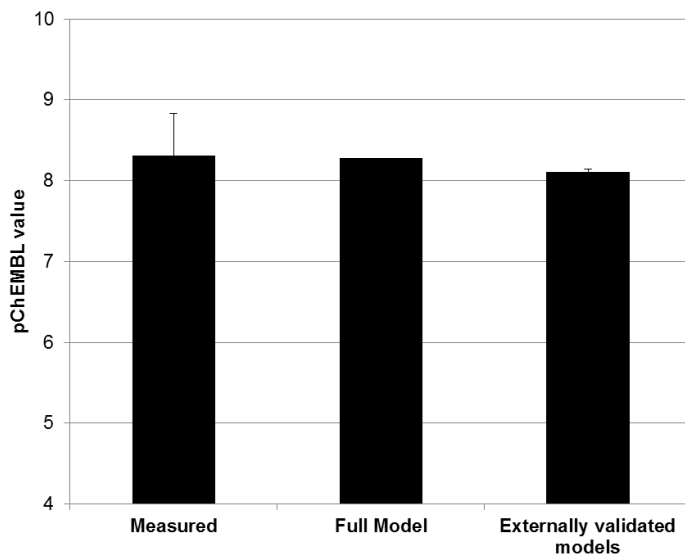


Figure S1. All model predictions for the binding affinity of Rimonabant at the CB1 receptor fall within measured range. The average pChEMBL value and the standard deviation are reported. Measured pChEMBL values include all the reported pChEMBL values for Rimonabant at the CB1 receptor in the ChEMBL database after filtering to obtain a high-quality dataset. Measured: average pChEMBL value is 8.3 with a standard deviation of 0.52. The full model predicted a pChEMBL value of 8.28 for Rimonabant at the CB1 receptor. The average pChEMBL value as predicted by the externally validated models is 8.11 with a standard deviation of 0.03.

Supplemental 5

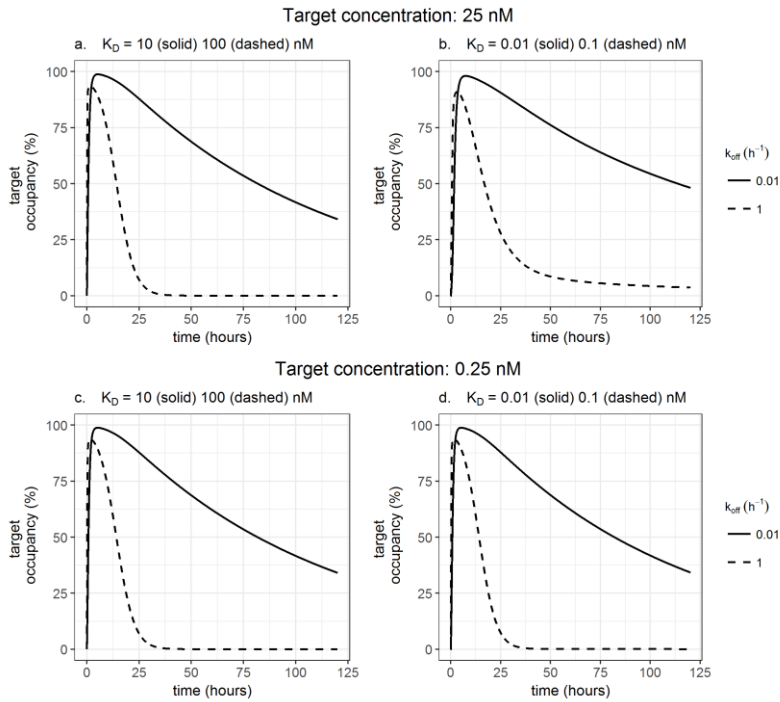


Figure S2. Target concentration and K_D determine the extent of in vivo kinetic target selectivity in Model 1. Target selectivity is characterised by a difference in target occupancy between target 1 (solid) and target 2 (dashed). The parameter values for these simulations can be found in Supplemental 1.

Supplemental 6

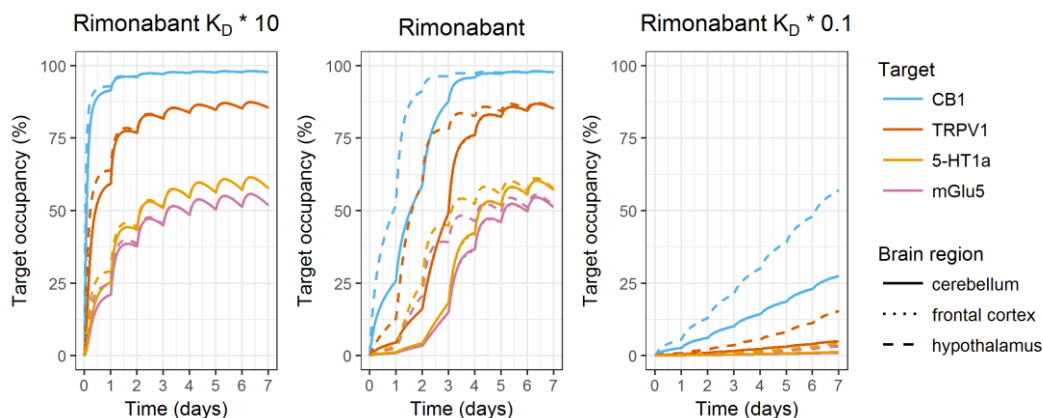


Figure S3. The simulated influence of K_D on the Rimonabant selectivity profile in Model III. Predicted K_D values of Rimonabant at the CB1, 5-HT1a, mGlu5 and TRPV1 receptor were used in these simulations, and multiplied by 10 or 0.1. k_{off} values were assumed to be 10 h^{-1} . A dose of 10^4 nmol was administered every 24 hours. $R_{tot,cer,CB1} = 527 \text{ nM}$, $R_{tot,cer,mGlu5} = 5.1 \text{ nM}$, $R_{tot,cer,TRPV1} = 19 \text{ nM}$, $R_{tot,cer,5-HT1a} = 0.01$, $R_{tot,hyp,CB1} = 248 \text{ nM}$, $R_{tot,hyp,mGlu5} = 16 \text{ nM}$, $R_{tot,hyp,TRPV1} = 13 \text{ nM}$, $R_{tot,hyp,5-HT1a} = 2.37$, $R_{tot,fc,CB1} = 529 \text{ nM}$, $R_{tot,fc,mGlu5} = 25 \text{ nM}$, $R_{tot,fc,TRPV1} = 12 \text{ nM}$, $R_{tot,fc,5-HT1a} = 1.7$.

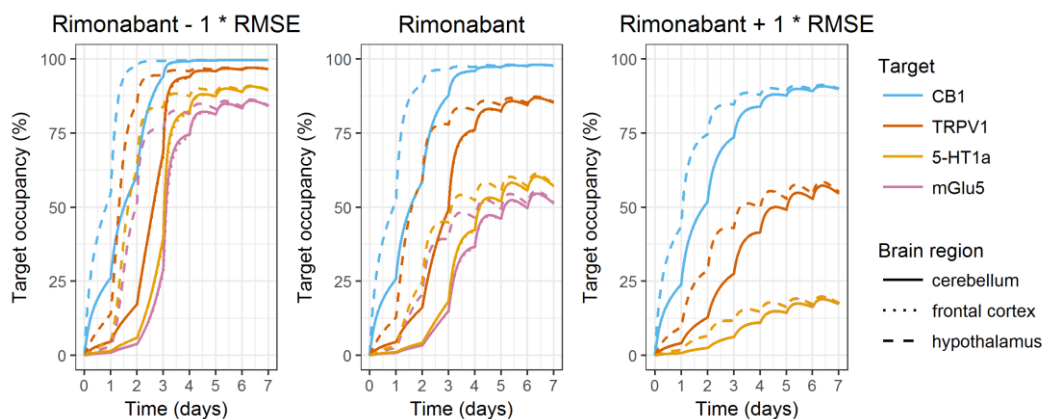


Figure S4. The influence of prediction errors on the simulated Rimonabant selectivity profile in Model III. Predicted K_D values of Rimonabant at the CB1, 5-HT1a, mGlu5 and TRPV1 receptor were used in these simulations. The RMSE values obtained from the external model validation of the QSAR were added or subtracted from the predicted pChEMBL value and then converted to the K_D value in nM ($10^{-pChEMBL \text{ value}} * 10^9$). k_{off} values were assumed to be 10 h^{-1} . A dose of 10^4 nmol was administered every 24 hours. $R_{tot,cer,CB1} = 527 \text{ nM}$, $R_{tot,cer,mGlu5} = 5.1 \text{ nM}$, $R_{tot,cer,TRPV1} = 19 \text{ nM}$, $R_{tot,cer,5-HT1a} = 0.01$, $R_{tot,hyp,CB1} = 248 \text{ nM}$, $R_{tot,hyp,mGlu5} = 16 \text{ nM}$, $R_{tot,hyp,TRPV1} = 13 \text{ nM}$, $R_{tot,hyp,5-HT1a} = 2.37$, $R_{tot,fc,CB1} = 529 \text{ nM}$, $R_{tot,fc,mGlu5} = 25 \text{ nM}$, $R_{tot,fc,TRPV1} = 12 \text{ nM}$, $R_{tot,fc,5-HT1a} = 1.7$.